Prediction of a Stable Organic Metal-Free Porous Material as a Catalyst for Water-Splitting

Hengshuai Li [1,2,3,*], **Haiquan Hu** [3], **Chenglin Bai** [3] , **Chunjiang Bao** [1], **Cailong Liu** [3], **Qinglin Wang** [3], **Feng Guo** [3], **Zhenbao Feng** [3], **Hanwen Yu** [1], **Ming Chen** [2] **and Konggang Qu** [4,*]

1   School of Mechanical & Automotive Engineering, Liaocheng University, Liaocheng 252000, China; baochunjiang@lcu.edu.cn (C.B.); yuhanwen@lcu.edu.cn (H.Y.)
2   School of Physics, Shandong University, Jinan 250100, China; chenming@sdu.edu.cn
3   Shandong Key Laboratory of Optical Communication Science and Technology, School of Physics Science and Information Technology, Liaocheng University, Liaocheng 252000, China; huhq@lcu.edu.cn (H.H.); baichenglin@lcu.edu.cn (C.B.); cailong_liu@jlu.edu.cn (C.L.); wangqinglin@lcu.edu.cn (Q.W.); guofeng@lcu.edu.cn (F.G.); fengzhenbao@lcu.edu.cn (Z.F.)
4   School of Chemistry and Chemical Engineering, Liaocheng University, Liaocheng 252000, China
*   Correspondence: hengshuaili@sina.com (H.L.); qukonggang@lcu.edu.cn (K.Q.); Tel.: +86-134-7589-5656 (H.L.)

Abstract: It is of practical significance to find organic metal-free catalyst materials. We propose a new graphene-like carbon nitride structure, which was able to meet these requirements well. Its primitive cell consists of eight carbon atoms and six nitrogen atoms. Hence, we called this structure g–C_8N_6. The stability of the structure was verified by phonon spectroscopy and molecular dynamics simulations. Then its electronic structure was calculated, and its band edge position was compared with the redox potential of water. We analyzed its optical properties and electron–hole recombination rate. After the above analysis, it is predicted that it is a suitable photocatalyst material. To improve its photocatalytic performance, two methods were proposed: applied tensile force and multilayer stacking. Our research is instructive for the photocatalytic application of this kind of materials.

Keywords: graphene-like carbon nitride; electronic structure; photocatalyst; tensile strain; multilayer stacking

1. Introduction

Two problems have plagued people for a long time—the energy crisis and environmental pollution. Scientists have put much effort into solving these two problems. The development of hydrogen energy is promising [1]. If we can obtain much hydrogen, we can solve these two problems effectively.

Water-splitting to produce hydrogen using a photocatalyst is a feasible method [2]. In 1972, Honda and Fujishima first produced H_2 by photochemical water-splitting using TiO_2 [3]. With development of technology, there are increasing kinds of photocatalysts, including various oxides, sulfides, oxynitride semiconductors, etc. [4–12], which belong to inorganic materials. Inorganic photocatalysts materials have some drawbacks, for example limited concentration of active sites and heavy metal toxicity [13–15]. However, organic photocatalysts have some merits, for example low cost, ease of fabrication and mechanical flexibility [16,17]. Therefore, research of metal-free organic high-efficiency photocatalysts is very important.

Since the exfoliation of monolayer graphene, two-dimensional materials have attracted comprehensive research for excellent properties [18–25]. It is increasingly important to study and regulate the properties of two-dimensional materials [26–28]. Wang et al. first considered

graphene-like carbon nitride (g–C_3N_4) as a photocatalyst. They predicted that the g–C_3N_4 photocatalyst exhibits interesting electronic properties that can decompose water to produce hydrogen [29]. Subsequently, many studies were carried out on the application of graphene-like carbon nitride in photocatalysis [30–36].

In this work, we propose a graphene-like carbon nitride structure with a primitive cell that consists of eight carbon atoms and six nitrogen atoms. Hence, we call this structure g–C_8N_6. First using basic calculations, we analyzed the electronic structure of g–C_8N_6 and compared its band edge position with the redox potential of water. At the same time, we calculated its optical properties and considered it as a suitable photocatalyst material.

2. Results and Discussion

The structure of the g–C_8N_6 supercell (3 × 3 × 1) is shown as Figure 1a. The primitive cell is marked using the yellow shaded area. The lattice constant is 7.177 Å, and the lengths of two types C–N bonds are 1.35 Å and 1.34 Å, respectively. Unlike many carbon nitrides, the s-heptazines in g–C_8N_6 is connected by C–C bonds, rather than C–N bonds. The lengths of the C–C bonds in the s-heptazines are 1.426 Å, however the length of C–C bonds between two connected s-heptazines are 1.439 Å. It has a very uniform hexagonal symmetry structure; which angles are all 120°. Because it has many holes, it has enough contact with water when it is used as a photocatalyst.
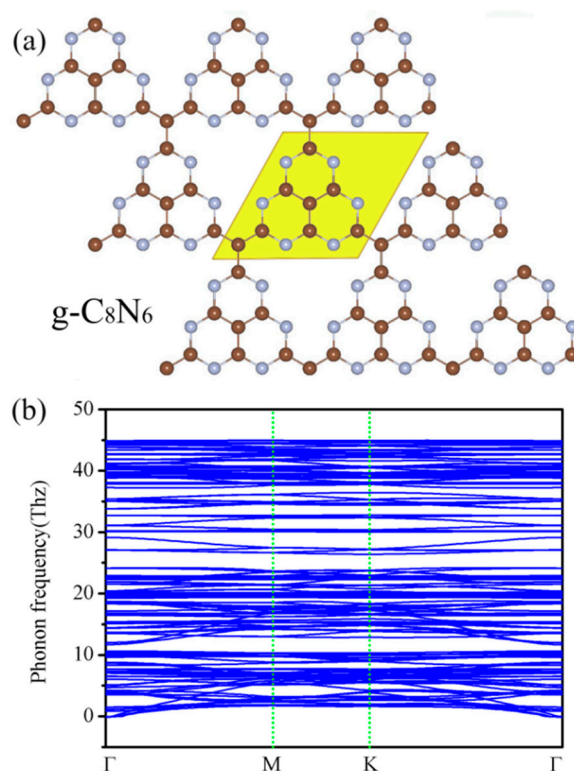
Figure 1. (**a**) Atomic structure of g–C_8N_6 supercell (3 × 3 × 1), the primitive cell is marked using the yellow shaded area, brown atoms are C and gray atoms are N; (**b**) phonon spectral dispersion diagram of g–C_8N_6 supercell (2 × 2 × 1).

Many similar carbon nitride structures have been synthesized [37–39], so perhaps a carbon-rich g–C_8N_6 layered structure may exhibit sufficient stability to be synthesized in future. We checked the stability of the structure theoretically through two methods. First, the force constant theory tested kinetic stability of the g–C_8N_6 through the phonon spectrum. A large (2 × 2) supercell was optimized in the calculation. The phonon spectral dispersion diagram along the highly symmetric direction in Brillouin zone is shown in Figure 1b. Obviously, the phonon spectral dispersion has no imaginary

frequency, indicating that g–C$_8$N$_6$ framework is kinetically stable. This is similar to the phonon spectra of g–C$_{13}$N$_{13}$ [28], C$_2$ N-*h*2D [40].

Second, the dynamic stability was checked with molecular dynamics simulations. The 126 atoms of the 3 × 3 supercell were simulated using a Nosé–Hoover thermostat at 300 K. The structure remained well after 5 ps, indicating its stability at room temperature. Temperature and total energy varied slightly with time, but the geometry of g–C$_8$N$_6$ remained stable.

Next, the electronic structures were analyzed. The energy-band structure distributions and electron density of states (DOS) by PBE method of g–C$_8$N$_6$ are shown in Figure 2a,b. It can be obtained that this material is a 2.13-eV band-gap semiconductor without magnetism. The conduction band minimum (CBM) is situated on K point and the valence band maximum (VBM) is situated on M point, which shows that g–C$_8$N$_6$ is an indirect band-gap semiconductor.
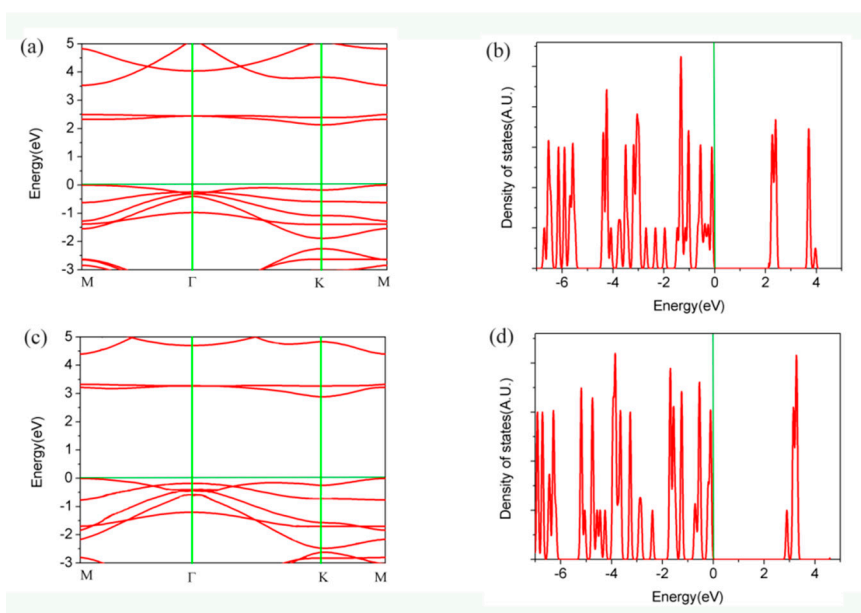
Figure 2. (**a**) Energy-band structure distributions and (**b**) electron density of states (DOS) of g–C$_8$N$_6$ by PBE method; (**c**) energy-band structure distributions and (**d**) electron density of states (DOS) of g–C$_8$N$_6$ by the HSE06 hybrid function method.

According to electronic structure of the material, we analyzed whether it is suitable for splitting water as a photocatalyst. The band of a photocatalyst should be greater than 1.23 eV, which is the difference between the water reduction potential and water oxidation potential. The positions of the conduction and valence band edges should straddle the redox potentials for water photolysis. The optical absorption properties should show that it can absorb partial visible light [41].

The band-edge potential affects whether it can be a photocatalyst. The CBM minus the Fermi energy and then minus the vacuum energy level is the conduction band edge. The VBM minus the Fermi energy and then minus the vacuum energy level is the valence band edge. The redox potentials of water are −4.5 eV and −5.73 eV, respectively. The conduction band edge of a suitable photocatalyst should be above the energy corresponding to the water reduction potential [ϕ(H$^+$/H$_2$)]. At the same time, the valence band edge of a suitable photocatalyst should be below the energy of the water oxidation potential [ϕ(O$_2$ /H$_2$O)]. As shown in Figure 3a, band gap of the g–C$_8$N$_6$ is 2.89 eV, which has ideal positions of the CBM and the VBM (E$_{CBM}$ = 1.22 eV and E$_{VBM}$ = 0.44 eV vs the normal hydrogen electrode, pH = 0). In other words, the electrons in the lowest unoccupied molecular orbital (LUMO) have sufficient reactivity to reduce water to hydrogen, whereas holes in the highest occupied molecular orbital (HOMO) have sufficient reduction potential to oxidize water to oxygen.
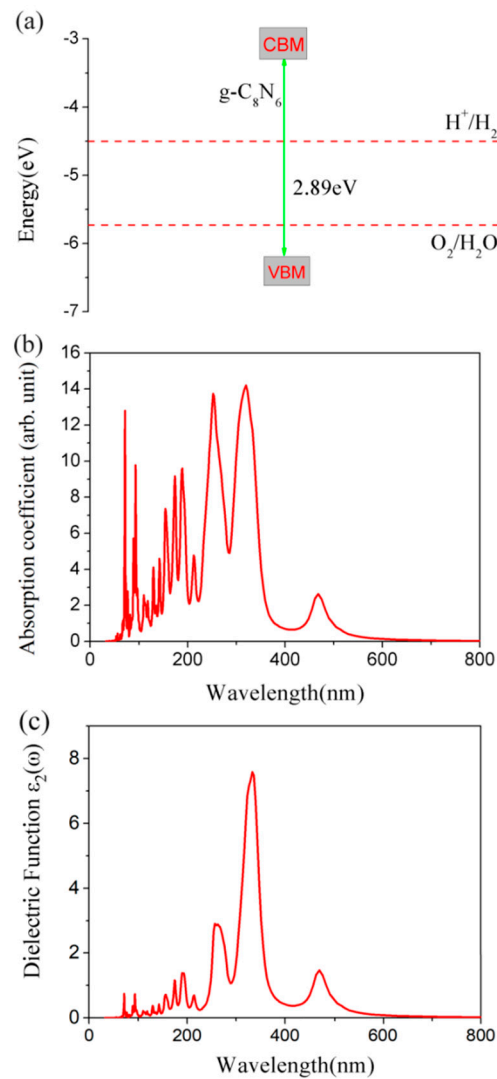
Figure 3. (**a**) Band alignments of g–C$_8$N$_6$ with respect to the standard water redox potentials; (**b**) absorption coefficient and (**c**) imaginary part of the dielectric function (in-plane polarization) for g–C$_8$N$_6$ using HSE06 method.

In order to analyze optical absorption properties of g–C$_8$N$_6$, we calculated the frequency-dependent dielectric matrix using hybrid HSE06 function and expanded a $10 \times 10 \times 1$ k-point mesh. The random phase approximation was used during the calculation of the frequency dependent dielectric tensor. The complex dielectric constants at a given frequency can be defined as:

$$\varepsilon(\omega) = \varepsilon_1(\omega) + i\varepsilon_2(\omega) \tag{1}$$

The expression for the absorption coefficient $I(\omega)$ is given as [42]:

$$I(\omega) = \omega\varepsilon_2/(cn) \tag{2}$$

where c is the speed of light, and n is the index of refraction:

$$n = \left[\sqrt{\varepsilon_1^2(\omega) + \varepsilon_2^2(\omega)} + \varepsilon_1(\omega) \right]^{1/2} / \sqrt{2} \tag{3}$$

According to the above equation, the light absorption property can be obtained mainly from the value of the imaginary part, and slightly from the value of the real part. The absorption coefficient was above zero, when only if the imaginary part:

$$\varepsilon_2(\omega) > 0 \tag{4}$$

The imaginary part is determined by the summation on the empty state. The following equation can be used:

$$\varepsilon_{\alpha\beta}^{(2)}(\omega) = \frac{4\pi^2 e^2}{\Omega} \lim_{q \to 0} \frac{1}{q^2} \sum_{c,v,\vec{k}} 2w_{\vec{k}} \delta(\varepsilon_{c\vec{k}} - \varepsilon_{v\vec{k}} - \omega)$$
$$\times \left\langle u_{c\vec{k}+e_\alpha\vec{q}} \middle| u_{v\vec{k}} \right\rangle \left\langle u_{c\vec{k}+e_\beta\vec{q}} \middle| u_{v\vec{k}} \right\rangle^* \tag{5}$$

where the indices c and v represent the conduction and valence band states and $u_{c\vec{k}}$ is the cell periodic part of the orbitals at the k point. The summation of Equation (4) includes a large number of empty conduction band states. The number of empty conduction band states is almost twice the number of valence bands.

According to the theory described above, frequency-dependent dielectric function of g–C_8N_6 was calculated by the hybrid HSE06 function. Figure 3b shows the absorption coefficient and Figure 3c shows imaginary part of dielectric function of g–C_8N_6. From Figure 3b,c, the solar spectral range which can be absorbed is from 60 nm to 600 nm. Hence, it is obvious that g–C_8N_6 can be used as a photocatalyst for splitting water.

The recombination rate of electron–hole is an important aspect affecting the photocatalytic performance. In the process of photocatalytic water-splitting, after electronic transition, electrons and holes will decompose water into hydrogen and oxygen. However, there are many electrons that will go back to original orbitals and recombine with holes. If recombination rate of electrons and holes is relatively low, then there will be more electrons involved in the redox reaction process, and the catalytic performance will be improved.

Figure 4a is the charge density of the conduction band minimum (CBM), which is situated on K point of the 32nd energy band. Figure 4b is the charge density of the valence band maximum (VBM), which is located on M point of the 31st energy band. Comparing Figure 4a,b, we can find that there are few overlapping parts in the distribution of charge density, that is, the recombination rate of electrons and holes is relatively low. This result indicates that g–C_8N_6 may exhibit long-lived electrons and holes that can improve its photocatalytic performance.

The g–C_8N_6 is a semiconductor with a suitable band gap. Its band edge position relative to the redox potential of water is ideal and can absorb a part of visible light. More valuable, the recombination rate of its electron holes is relatively low. In summary, it has characteristics of photocatalyst and can be used for water-splitting.

Next, we analyze whether there are some ways to improve its performance. As we all know, tensile strain can regulate electronic structure of material and thus improves its properties [28,38,43]. Hence, we applied tensile strain to g–C_8N_6 to observe its band-gap change. Tensile strain is defined as:

$$\varepsilon = \frac{l - l_0}{l_0} \times 100\% \tag{6}$$

where l_0 is length of original supercell structure, and l is length of supercell under tensile strain.

Figure 5 is the case of band-gap changes as the tensile force changes with PBE functional. The color of the squares in figure represents the color of the solar spectrum that can be absorbed. With the increase of tensile force, the length of C–C bonds and C–N bonds gradually increases, indicating that the orbitals binding ability of these bonds is weakened. At the same time, the splitting of bonding and antibonding decreases, resulting in narrow band gap, so absorption range of sunlight extends to

green region. In contrast, when compressive stress is applied, the splitting of bonding and antibonding increases, thus widened the band gap, and the absorption of sunlight moves to red region. To sum up these two cases, tensile force can be used to capture a wider spectrum of the sun.
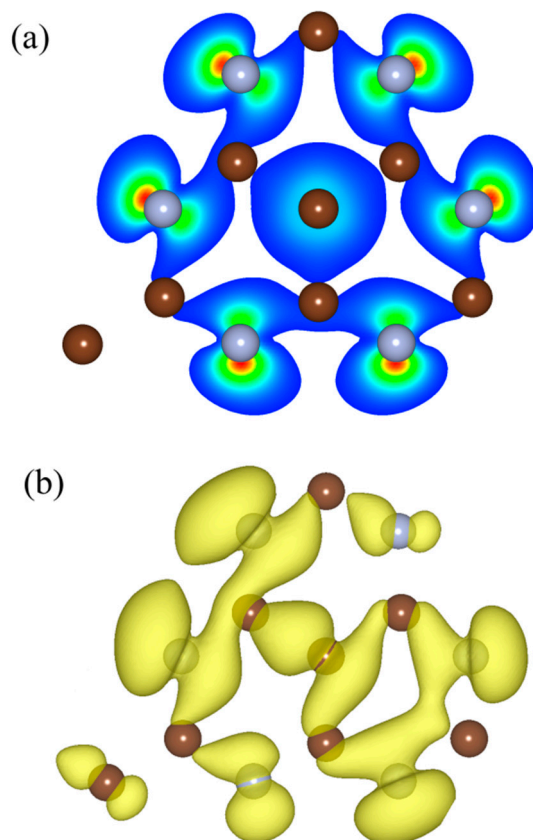
Figure 4. (**a**) Charge density of the conduction band minimum (CBM), which is located on K point of the 32nd energy band; (**b**) charge density of the valence band maximum (VBM), which is located on M point of the 31st energy band. The isosurface value is set to 0.003 $Å^{-3}$.
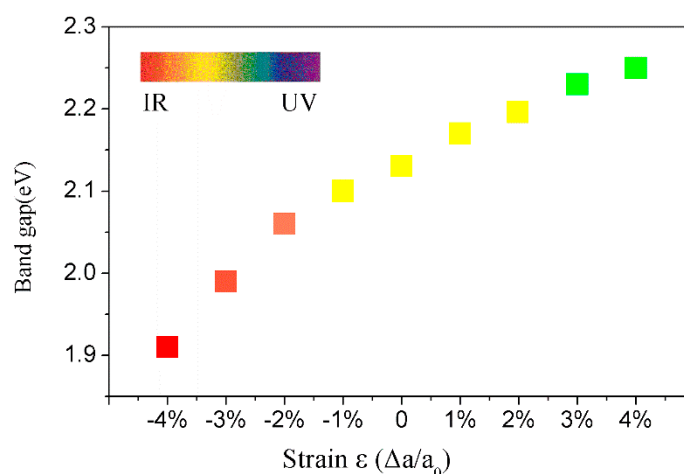
Figure 5. Case of band-gap changes as the tensile force changes. The color of the squares in figure represents the color of the solar spectrum that should be absorbed.

Multilayer stacking can also adjust electronic structure of material, thus improving its performance [44]. The multilayer structure is AA stacking. Work functions and energy-band gap of two-, three-, four-, five- and six-layer g–C_8N_6 calculated are listed in Table 1 with HSE06 functional.

This is particularly important for layered structures as the interlayer interaction depends on the van der Waals interaction [45,46]. The results of Table 1 and Figure 6 were calculated using van der Waals force. Although the number of layers is increasing gradually, the work function maintain stability. In sharp contrast band gap decreases gradually with increase of the number of layers. Similar to the monolayer, all multilayer g–C_8N_6 remain an indirect gap semiconductor. When the number of layers is 2–6, the band gap is 2.50–2.35 eV. As number of layers increases, properties of the material gradually approach the bulk material with a gap of 2.35 eV. Compared with single-layer, multilayer stacking reduced the band gap by 0.54 eV.

Table 1. Work function (WF) and band gap (Eg) of two-, three-, four-, five- and six-layer 2D g–C_8N_6 computed with HSE06 functional. The band-gap differences (ΔEg) between the multilayers and mono-layer g–C_8N_6 are shown.

N	1	2	3	4	5	6	N
WF (eV)	5.30	5.28	5.30	5.26	5.29	5.30	5.30
Eg (eV)	2.89	2.50	2.40	2.38	2.36	2.35	2.35
ΔEg (eV)	0.00	0.39	0.49	0.51	0.53	0.54	0.54
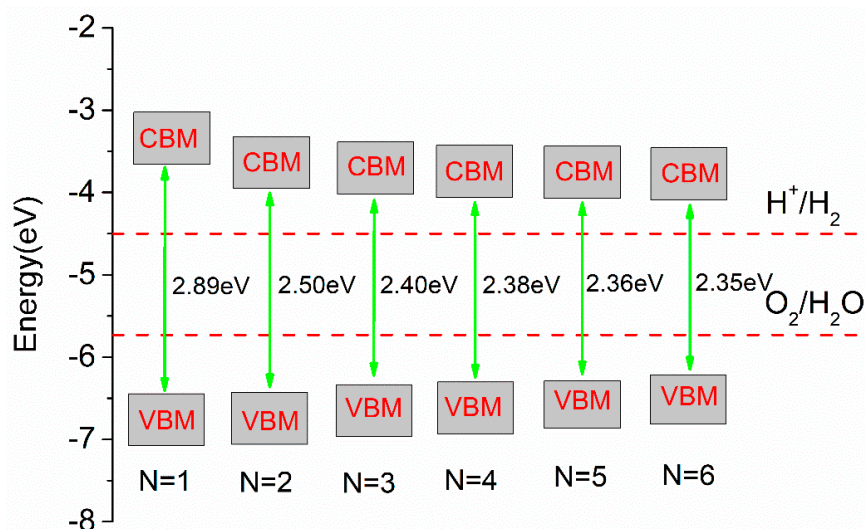
Figure 6. Band-edge potentials of multilayer g–C_8N_6 compare to standard water redox potentials.

To study the photocatalytic capacity of multilayer g–C_8N_6, the band alignment are shown in Figure 6. Compared with the monolayer, the VBM of the bilayer structure increased, while the CBM of the bilayer structure decreased. The other multilayer g–C_8N_6 systems were similar to the bilayer structure. The multilayered g–C_8N_6 system had ideal band edges that could decompose water to produce hydrogen and oxygen.

3. Method and Computational Details

The calculations were carried out within the framework of density functional theory (DFT), which was implemented in the Vienna ab initio simulation package known as VASP [47–49]. The electron–electron interactions were handled by exchange correlation functions with Perde–Burke–Ernzerhof (PBE) in the form of generalized gradient approximation (GGA) [50]. Energy cutoff value for plane wave expansion of electron wave function is set to 600 eV. Projector-augmented wave (PAW) potentials were used to describe electron–ion interactions [51,52]. Valence electrons include four electrons of carbon (2s22p2) and five electrons of nitrogen (2s22p3). A vacuum region was set to 15 Å. The Brillouin zone was divided into 9 × 9 × 1 k points. Structural optimization was performed by conjugate gradient (CG) method until the residual force of each atom was less than 0.001 eV/Å. A more accurate

Heyd–Scuseria–Ernzerhof (HSE) screening potential method [53,54] was used to calculate band gap. Optical absorption spectra of the two dimension covalent triazine frameworks (CTFs) were computed from the dielectric function by Kramers–Kronig dispersion relation [55]. Work function means the minimum energy that must be provided for an electron to escape immediately from the surface of the material. The work function can be calculated by: $\varphi = V(\infty) - E_F$, where $V(\infty)$ and E_F are the electrostatic potential in a vacuum region far from the neutral surface and the Fermi energy of the neutral surface system, respectively.

4. Conclusions

We propose a new graphene-like carbon nitride structure g–C_8N_6, the stability of the structure of which was verified by phonon spectroscopy and molecular dynamics simulations. Then its electronic structure was calculated, and its band edge position was compared with the redox potential of water. We analyzed its optical properties and electron–hole recombination rate. After the above analysis, it is theoretically a suitable water-splitting photocatalyst material. To improve its photocatalytic performance, two methods were proposed: applied tensile force and multilayer stacking. Our research is instructive for the photocatalytic application of this kind of materials.

Author Contributions: Conceptualization, H.L.; data curation, Q.W. and Z.F.; formal analysis, M.C.; funding acquisition, C.L.; resources, C.B. (Chunjiang Bao) and K.Q.; software, C.B. (Chenglin Bai) and F.G.; writing—original draft, H.Y.; writing—review & editing, H.H. All authors have read and agreed to the published version of the manuscript.

Funding: This research was funded by Introduction and Cultivation Plan of Youth Innovation Talents for Universities of Shandong Province in 2019 (Research and Innovation Team on Materials Modification and Optoelectronic Devices at extreme conditions), Shandong Provincial Key Research and Development Program (Public Welfare Science and Technology Research) (No. 2019GGX103010), Science and Technology Plan of Youth Innovation Team for Universities of Shandong Province (No. 2019KJJ019), Shandong Natural Science Foundation (No. ZR2019PEE006), National Natural Science Foundation of China (No. 11504153, 11504386), Science and Technology Planning Project of Higher School in Shandong Province (No. J18KA243) and Liaocheng University High-level Talents & PhD Research Startup Foundation (No. 318051619). The APC was funded by Introduction and Cultivation Plan of Youth Innovation Talents for Universities of Shandong Province in 2019 (Research and Innovation Team on Materials Modification and Optoelectronic Devices at extreme conditions).

Conflicts of Interest: The authors declare no conflict of interest.

References

1. Kroke, E.; Schwarz, M. Novel group 14 nitrides. *Coord. Chem. Rev.* **2004**, *248*, 493–532. [CrossRef]
2. Chen, X.; Shen, S.; Guo, L.; Mao, S.S. Semiconductor-based photocatalytic hydrogen generation. *Chem. Rev.* **2010**, *110*, 6503–6570. [CrossRef] [PubMed]
3. Fujishima, A.; Honda, K. Electrochemical photolysis of water at a semiconductor electrode. *Nature* **1972**, *238*, 37–38. [CrossRef] [PubMed]
4. Kumaravel, V.; Kang, M. Photocatalytic Hydrogen Evolution. *Catalysts* **2020**, *10*, 492. [CrossRef]
5. Ming, H.; Ming, J.; Oh, S.-M.; Lee, E.-J.; Huang, H.; Zhou, Q.; Zheng, J.; Sun, Y.-K. High dispersion of TiO_2 nanocrystals within porous carbon improves lithium storage capacity and can be applied batteries to $LiNi_{0.5}Mn_{1.5}O_4$. *J. Mater. Chem. A* **2014**, *2*, 18938–18945. [CrossRef]
6. Xu, L.; Cui, Q.; Zhang, H.; Jiao, A.; Tian, Y.; Li, S.; Li, H.; Chen, M.; Chen, F. Ultra-clean PtPd nanoflowers loaded on GO supports with enhanced low-temperature electrocatalytic activity for fuel cells in harsh environment. *Appl. Surf. Sci.* **2020**, *511*, 145603. [CrossRef]
7. Park, J.H.; Kim, S.; Bard, A.J. Novel carbon-doped TiO_2 nanotube arrays with high aspect ratios for efficient solar water splitting. *Nano Lett.* **2006**, *6*, 24–28. [CrossRef]
8. Hua, J.; Liu, Y.L.; Li, H.S.; Zhao, M.W.; Liu, X.D. Effect of the alloying element titanium on the stability and trapping of hydrogen in pure vanadium: A first-principles study. *Int. J. Mod. Phys. B* **2014**, *28*, 1450207. [CrossRef]
9. Ksibi, M.; Rossignol, S.; Tatibouët, J.-M.; Trapalis, C. Synthesis and solid characterization of nitrogen and sulfur-doped TiO_2 photocatalysts active under near visible light. *Mater. Lett.* **2008**, *62*, 4204–4206. [CrossRef]
10. Cheng, Y.W.; Chan, R.C.; Wong, P. Disinfection of Legionella pneumophila by photocatalytic oxidation. *Water Res.* **2007**, *41*, 842–852. [CrossRef]

11. Yu, J.; Xiang, Q.; Zhou, M. Preparation, characterization and visible-light-driven photocatalytic activity of Fe-doped titania nanorods and first-principles study for electronic structures. *Appl. Catal. B: Environ.* **2009**, *90*, 595–602. [CrossRef]

12. Liu, S.; Yu, J.; Jaroniec, M. Tunable photocatalytic selectivity of hollow TiO$_2$ microspheres composed of anatase polyhedra with exposed {001} facets. *J. Am. Chem. Soc.* **2010**, *132*, 11914–11916. [CrossRef] [PubMed]

13. Zhang, X.; Xie, X.; Wang, H.; Zhang, J.; Pan, B.; Xie, Y. Enhanced photoresponsive ultrathin graphitic-phase C$_3$N$_4$ nanosheets for bioimaging. *J. Am. Chem. Soc.* **2013**, *135*, 18–21. [CrossRef] [PubMed]

14. Su, D.S.; Zhang, J.; Frank, B.; Thomas, A.; Wang, X.; Paraknowitsch, J.; Schlögl, R. Metal-free heterogeneous catalysis for sustainable chemistry. *Chemsuschem: Chem. Sustain. Energy Mater.* **2010**, *3*, 169–180. [CrossRef]

15. Hua, J.; Liu, Y.L.; Li, H.S.; Zhao, M.W.; Liu, X.D. Energetics of carbon and nitrogen impurities and their interactions with vacancy in vanadium. *Chin. Phys. B* **2016**, *25*, 036104. [CrossRef]

16. Xiao, W.; Jin, X.; Chen, G.Z. Up-scalable and controllable electrolytic production of photo-responsive nanostructured silicon. *J. Mater. Chem. A* **2013**, *1*, 10243–10250. [CrossRef]

17. Ng, C.H.; Winther-Jensen, O.; Ohlin, C.A.; Winther-Jensen, B. Exploration and optimisation of poly (2, 2′-bithiophene) as a stable photo-electrocatalyst for hydrogen production. *J. Mater. Chem. A* **2015**, *3*, 11358–11366. [CrossRef]

18. Novoselov, K.S.; Geim, A.K.; Morozov, S.V.; Jiang, D.; Zhang, Y.; Dubonos, S.V.; Grigorieva, I.V.; Firsov, A.A. Electric field effect in atomically thin carbon films. *Science* **2004**, *306*, 666–669. [CrossRef]

19. Bunch, J.S.; Van Der Zande, A.M.; Verbridge, S.S.; Frank, I.W.; Tanenbaum, D.M.; Parpia, J.M.; Craighead, H.G.; McEuen, P.L. Electromechanical resonators from graphene sheets. *Science* **2007**, *315*, 490–493. [CrossRef]

20. Lee, C.; Wei, X.W.; Kysar, J.W.; Hone, J. Measurement of the elastic properties and intrinsic strength of monolayer grapheme. *Science* **2008**, *321*, 385–388. [CrossRef]

21. Meyer, J.C.; Geim, A.K.; Katsnelson, M.I.; Novoselov, K.S.; Booth, T.J.; Roth, S. The structure of suspended graphene sheets. *Nature* **2007**, *446*, 60. [CrossRef] [PubMed]

22. Novoselov, K.S.; Geim, A.K.; Morozov, S.V.; Jiang, D.; Katsnelson, M.I.; Grigorieva, I.V.; Dubonos, S.V.; Firsov, A.A. Two-dimensional gas of massless Dirac fermions in graphene. *Nature* **2005**, *438*, 197–200. [CrossRef] [PubMed]

23. Geim, A.K.; Novoselov, K.S. The rise of graphene. *Nat. Mater.* **2007**, *6*, 183. [CrossRef]

24. Li, H.; Hu, H.; Bao, C.; Zhang, X.; Wang, A.; Zhou, H.; Zhao, M. The strability and electronic structure of Fe atoms embedded in zigzag graphene nanoribbons. *Phys. B: Condens. Matter* **2014**, *441*, 28–32. [CrossRef]

25. Xu, M.; Liang, T.; Shi, M.; Chen, H. Graphene-like two-dimensional materials. *Chem. Rev.* **2013**, *113*, 3766–3798. [CrossRef]

26. Zhang, H.; Cui, Q.; Xu, L.; Jiao, A.; Tian, Y.; Liu, X.; Li, S.; Li, H.; Chen, M.; Chen, F. Blue laser-induced photochemical synthesis of CuAg nanoalloys on h-BN supports with enhanced SERS activity for trace-detection of residual pesticides on tomatoes. *J. Alloy. Compd.* **2020**, *825*, 153996. [CrossRef]

27. Saleem, Z.; Pervaiz, E.; Yousaf, M.U.; Niazi, M.B.K. Two-dimensional materials and composites as potential water splitting photocatalysts: A review. *Catalysts* **2020**, *10*, 464. [CrossRef]

28. Li, H.; Hu, H.; Bai, C.; Bao, C.; Feng, Z.; Guo, F. The metal-free magnetism and ferromagnetic narrow gap semiconductor properties in graphene-like carbon nitride. *Phys. B: Condens. Matter* **2019**, *555*, 91–95. [CrossRef]

29. Wang, X.; Maeda, K.; Thomas, A.; Takanabe, K.; Xin, G.; Carlsson, J.M.; Domen, K.; Antonietti, M. A metal-free polymeric photocatalyst for hydrogen production from water under visible light. *Nat. Mater.* **2009**, *8*, 76–80. [CrossRef]

30. Liu, G.; Niu, P.; Sun, C.; Smith, S.C.; Chen, Z.; Lu, G.Q.; Cheng, H.-M. Unique electronic structure induced high photoreactivity of sulfur-doped graphitic C$_3$N$_4$. *J. Am. Chem. Soc.* **2010**, *132*, 11642–11648. [CrossRef]

31. Zhang, J.; Sun, J.; Maeda, K.; Domen, K.; Liu, P.; Antonietti, M.; Fu, X.; Wang, X. Sulfur-mediated synthesis of carbon nitride: Band-gap engineering and improved functions for photocatalysis. *Energy Environ. Sci.* **2011**, *4*, 675–678. [CrossRef]

32. Wu, F.; Liu, Y.; Yu, G.; Shen, D.; Wang, Y.; Kan, E. Visible-light-absorption in graphitic C$_3$N$_4$ bilayer: Enhanced by interlayer coupling. *J. Phys. Chem. Lett.* **2012**, *3*, 3330–3334. [CrossRef]

33. Maeda, K.; Wang, X.; Nishihara, Y.; Lu, D.; Antonietti, M.; Domen, K. Photocatalytic activities of graphitic carbon nitride powder for water reduction and oxidation under visible light. *J. Phys. Chem. C* **2009**, *113*, 4940–4947. [CrossRef]

34. Zhu, Y.-P.; Li, M.; Liu, Y.-L.; Ren, T.-Z.; Yuan, Z.-Y. Carbon-doped ZnO hybridized homogeneously with graphitic carbon nitride nanocomposites for photocatalysis. *J. Phys. Chem. C* **2014**, *118*, 10963–10971. [CrossRef]

35. Du, A.; Sanvito, S.; Li, Z.; Wang, D.; Jiao, Y.; Liao, T.; Sun, Q.; Ng, Y.H.; Zhu, Z.; Amal, R. Hybrid graphene and graphitic carbon nitride nanocomposite: Gap opening, electron–hole puddle, interfacial charge transfer, and enhanced visible light response. *J. Am. Chem. Soc.* **2012**, *134*, 4393–4397. [CrossRef]

36. Takanabe, K.; Kamata, K.; Wang, X.; Antonietti, M.; Kubota, J.; Domen, K. Photocatalytic hydrogen evolution on dye-sensitized mesoporous carbon nitride photocatalyst with magnesium phthalocyanine. *Phys. Chem. Chem. Phys.* **2010**, *12*, 13020–13025. [CrossRef]

37. Suter, T.M.; Brazdova, V.; Mccoll, K.; Miller, T.S.; Nagashima, H.; Salvadori, E.; Sella, A.; Howard, C.H.; Kay, C.W.M.; Cora, F.; et al. Synthesis, structure and electronic properties of graphitic carbon nitride films. *J. Phys. Chem. C* **2018**, *122*, 25183–25194. [CrossRef]

38. Li, H.; Hu, H.; Bao, C.; Hua, J.; Zhou, H.; Liu, X.; Liu, X.; Zhao, M. Tensile strain induced half-metallicity in graphene-like carbon nitride. *Phys. Chem. Chem. Phys.* **2015**, *17*, 6028–6035. [CrossRef]

39. Mahmood, J.; Lee, E.K.; Jung, M.; Shin, D.; Jeon, I.-Y.; Jung, S.-M.; Choi, H.-J.; Seo, J.-M.; Bae, S.-Y.; Sohn, S.-D. Nitrogenated holey two-dimensional structures. *Nat. Commun.* **2015**, *6*, 6486. [CrossRef]

40. Li, H.; Hu, H.; Bao, C.; Feng, Z.; Guo, F.; Tian, G.; Liu, Y. Potential application of a porous graphitic carbon nitride as an organic metal-free photocatalyst for water splitting. *Diam. Relat. Mater.* **2018**, *87*, 50–55. [CrossRef]

41. Li, H.; Hu, H.; Bao, C.; Guo, F.; Zhang, X.; Liu, X.; Hua, J.; Tan, J.; Wang, A.; Zhou, H. Forming heterojunction: An effective strategy to enhance the photocatalytic efficiency of a new metal-free organic photocatalyst for water splitting. *Sci. Rep.* **2016**, *6*, 29327. [CrossRef] [PubMed]

42. Guan, S.; Cheng, Y.; Liu, C.; Han, J.; Lu, Y.; Yang, S.A.; Yao, Y. Effects of strain on electronic and optic properties of holey two-dimensional C2N crystals. *Appl. Phys. Lett.* **2015**, *107*, 231904. [CrossRef]

43. Li, H.; Hu, H.; Bai, C.; Bao, C.; Guo, F.; Feng, Z.; Liu, Y. The charge regulation of electronic structure and optical properties of graphitic carbon nitride under strain. *Rsc. Adv.* **2019**, *9*, 7464–7468. [CrossRef]

44. Yang, G.; Li, L.; Lee, W.B.; Ng, M.C. Structure of graphene and its disorders: A review. *Sci. Technol. Adv. Mater.* **2018**, *19*, 613–648. [CrossRef]

45. Van, T.B.; Torrent, M.; Gonze, X. Interatomic force constants including the DFT-D dispersion contribution. *Phys. Rev. B* **2016**, *93*, 144304.

46. Pike, N.; Dewandre, A.; Van Troeye, B.; Gonze, X.; Verstraete, M. Vibrational and dielectric properties of the bulk transition metal dichalcogenides. *Phys. Rev. Mater.* **2018**, *2*, 063608. [CrossRef]

47. Kresse, G.; Hafner, J. Ab initio molecular dynamics for liquid metals. *Phys. Rev. B* **1993**, *47*, 558. [CrossRef]

48. Kresse, G.; Hafner, J. Ab initio molecular-dynamics simulation of the liquid-metal–amorphous-semiconductor transition in germanium. *Phys. Rev. B* **1994**, *49*, 14251. [CrossRef]

49. Kresse, G.; Furthmüller, J. Efficient iterative schemes for ab initio total-energy calculations using a plane-wave basis set. *Phys. Rev. B* **1996**, *54*, 11169. [CrossRef]

50. Perdew, J.P.; Burke, K.; Ernzerhof, M. Generalized gradient approximation made simple. *Phys. Rev. Lett.* **1996**, *77*, 3865. [CrossRef]

51. Blöchl, P.E. Projector augmented-wave method. *Phys. Rev. B* **1994**, *50*, 17953.

52. Kresse, G.; Joubert, D. From ultrasoft pseudopotentials to the projector augmented-wave method. *Phys. Rev. B* **1999**, *59*, 1758. [CrossRef]

53. Heyd, J.; Scuseria, G.E.; Ernzerhof, M. Hybrid functionals based on a screened Coulomb potential. *J. Chem. Phys.* **2003**, *118*, 8207–8215. [CrossRef]

54. Heyd, J.; Scuseria, G.E. Efficient hybrid density functional calculations in solids: Assessment of the Heyd–Scuseria–Ernzerhof screened Coulomb hybrid functional. *J. Chem. Phys.* **2004**, *121*, 1187–1192. [CrossRef] [PubMed]

55. Gajdoš, M.; Hummer, K.; Kresse, G.; Furthmüller, J.; Bechstedt, F. Linear optical properties in the projector-augmented wave methodology. *Phys. Rev. B* **2006**, *73*, 045112.